

1
2
3
4
5
6
7
8
9
10
11
12
13
14
15
16
17
18
19
20
21
22
23
24
25

Ultrastructure of light-activated axons following optogenetic stimulation to produce late-phase long-term
potentiation

Masaaki Kuwajima^{1¶}, Olga I. Ostrovskaya^{1¶}, Guan Cao¹, Seth A. Weisberg², *Kristen M. Harris^{1,2}, *Boris V.
Zemelman^{1,2}

¹Center for Learning and Memory, The University of Texas at Austin, Austin, Texas, United States of America

²Department of Neuroscience, The University of Texas at Austin, Austin, Texas, United States of America

*Corresponding authors

E-mail: kharris@mail.clm.utexas.edu (KMH) and zemelmanb@mail.clm.utexas.edu (BVZ)

¶These authors contributed equally to this work.

Short title: Ultrastructure of optogenetically produced L-LTP

26 **Abstract**

27 Analysis of neuronal compartments has revealed many state-dependent changes in geometry but establishing
28 synapse-specific mechanisms at the nanoscale has proven elusive. We co-expressed channelrhodopsin2-GFP
29 and mAPEX2 in a subset of hippocampal CA3 neurons and used trains of light to induce late-phase long-term
30 potentiation (L-LTP) in area CA1. L-LTP was shown to be specific to the labeled axons by severing CA3 inputs,
31 which prevented back-propagating recruitment of unlabeled axons. Membrane-associated mAPEX2 tolerated
32 microwave-enhanced chemical fixation and drove tyramide signal amplification to deposit Alexa Fluor dyes in
33 the light-activated axons. Subsequent post-embedding immunogold labeling resulted in outstanding
34 ultrastructure and clear distinctions between labeled (activated), and unlabeled axons without obscuring
35 subcellular organelles. The gold-labeled axons in potentiated slices were reconstructed through serial section
36 electron microscopy; presynaptic vesicles and other constituents could be quantified unambiguously. The
37 genetic specification, reliable physiology, and compatibility with established methods for ultrastructural
38 preservation make this an ideal approach to link synapse ultrastructure and function in intact circuits.

39

40 Introduction

41 The cellular correlates of learning and memory have been the subjects of intense study and
42 speculation. We and others have used patterns of activity that produce late-phase long-term potentiation (L-
43 LTP), a form of synaptic plasticity resulting in an increased synaptic efficacy. L-LTP is protein synthesis
44 dependent and lasts more than three hours. Although some structural changes occur early following the
45 induction of LTP, the lasting changes are most likely to reflect mechanisms of memory. *Post hoc* three-
46 dimensional reconstruction from serial section electron microscopy (3DEM) of synapses and resident
47 structures has revealed alterations that occur and are sustained long after the induction of LTP [1–4].
48 Mechanistic interpretation has been limited, however, because it has only been possible to compare
49 subpopulations of synapses near LTP-producing versus control sites, rather than identify potentiated
50 synapses. Genetic targeting to tag and stimulate individual cells can be achieved by co-expressing
51 channelrhodopsin2 (ChR2) and a modified ascorbate peroxidase [5,6]. Here, we adapted this approach to
52 potentiate a subset of CA3→CA1 hippocampal axons and to identify synapses recently involved in L-LTP.

53 Optical modulation of plasticity is routinely used across brain areas, and *in vivo* experiments have
54 revealed a correlation between behavioral memory and optically-induced synaptic plasticity (LTP and long-term
55 depression [LTD]) [7,8]. In slice preparations, past efforts using various protocols to induce LTP using ChR2
56 have been limited to whole-cell recordings and short post-induction times [9–12]. In the hippocampal
57 CA3→CA1 pathway, a previous study used optical stimulation to induce late-phase LTD *in vivo* [13]; however,
58 in this pathway, optically induced L-LTP to our knowledge has not been demonstrated.

59 We expressed ChR2 and labeled a subset of CA3→CA1 Schaffer collateral and commissural fiber
60 axons using a single virus and then produced L-LTP using high-frequency light pulses. This approach
61 generated a mosaic of labeled and unlabeled axons and allowed a within-preparation comparison of identified
62 synapses having distinct histories of activation. As proof of concept, we reconstructed a labeled axon through
63 3DEM from a slice that displayed optically induced L-LTP. The tissue quality was superb, demonstrating that
64 we could identify genetically tagged activated axons. The approach proved compatible with conventional tissue
65 fixation and the processing methods needed to preserve subcellular organelles. Hence, it provides a reliable
66 strategy to study synapse-specific mechanisms of synaptic plasticity.

67 **Materials and methods**

68 **Animals**

69 This study was carried out in accordance with the recommendations in the Guide for the Care and Use
70 of Laboratory Animals of the National Institutes of Health. All animal procedures were approved by the
71 University of Texas at Austin Animal Care and Use Committee (protocol number AUP-2012-00056 and its
72 successors). All mice were housed under reversed light/dark cycles in an AAALAC-accredited facility managed
73 by the University of Texas Animal Resource Center. We used 8-12 week old male 129S6/SvEvTac mice
74 (Taconic Biosciences, RRID:IMSR_TAC:129sve) for all LTP experiments. Male C57B/6J mice (The Jackson
75 Laboratory, RRID:IMSR_JAX:000664) were also used for earlier experiments, which are indicated as such in
76 figure captions where applicable. All efforts were made to minimize suffering.

78 **AAV assembly and production**

79 A channelrhodopsin2^{ET/TC} [14] fusion protein was assembled with superfolder green fluorescent protein
80 (GFP) [15] fitted with C-terminal Kir2.1 ER export signal [16]. To generate mAPEX2, we modified the wild type
81 ascorbate peroxidase from *P. sativum* (APX) [17] to include an N-terminal palmitoylation tag from growth-
82 associated protein 43 (GAP-43) [18], amino acid substitutions K14D, W41F, E112K [5], and A134P [6], and a
83 C-terminal hemagglutinin epitope tag (HA tag: YPYDVPDYA). Chr2 and codon-optimized mAPEX2 were
84 separated by the self-cleaving porcine teschovirus P2A peptide [19] to produce both proteins from a single
85 transcript. In earlier experiments, we used a version of the rAAV that encoded myc-tagged mAPEX1 with the
86 first three mutations instead of mAPEX2 (indicated in figure captions where applicable).

87 In addition to the two proteins, the recombinant adeno-associated virus (rAAV) construct comprised an
88 enhanced human synapsin promoter [20], the woodchuck post-transcriptional regulatory element and SV40
89 polyadenylation sequence. Viruses were assembled using a modified helper-free system (Stratagene) as
90 serotype 2/1 (*rep/cap*) and purified on sequential cesium gradients according to published methods [21]. Titers
91 were measured using a payload-independent qPCR technique [22]. Typical titers were $>10^{10}$ viral genomes/ μ l.

92

93 **Rat hippocampal neurons**

94 Hippocampal neurons obtained from rats (embryonic day 19) were grown in dissociated cultures [23] on
95 coverslips and were infected on day 8 after plating with the rAAV construct encoding mAPEX1. At 6-10 days
96 post-infection, the neurons used for immunostaining were fixed with 4% formaldehyde in phosphate-buffered
97 saline (PBS) for 15 min. For labeling with 3,3'-diaminobenzidine (DAB; Sigma-Aldrich), the neurons were fixed
98 for 30 min with 2% formaldehyde and 6% glutaraldehyde. All glutaraldehyde-containing fixative was prepared
99 in 0.1 M sodium cacodylate buffer (pH = 7.4) with 2 mM CaCl₂ and 4 mM MgSO₄.

100 **Stereotaxic injections**

101 Mice under isoflurane anesthesia (1-4% mixed in O₂) were placed in a stereotaxic apparatus and
102 prepared for injections with craniotomies over the hippocampal area CA3. Unilateral injections were performed
103 using a pulled glass pipette (10-15 μm diameter tip) mounted on a Nanoject II small-volume injector
104 (Drummond Scientific). Approximately 30 nl of virus was deposited at each injection site at 1-2 minute intervals
105 (from bregma in mm: AP +1.9, ML -2.3, DV 1.8, 1.6, 1.4; AP +2.1, ML -2.5, DV 1.8, 1.6, 1.4). The pipette was
106 left in place for 3–5 min before being removed from the brain. Carprofen (5 mg/kg, sc; TW Medical Cat# PF-
107 8507) was injected 20 min before the end of surgery, and mice were monitored daily thereafter to ensure full
108 recovery. Two rAAV-injected mice (129S6/SvEvTac) were perfusion-fixed under heavy isoflurane anesthesia
109 with 4% paraformaldehyde in 0.02 M phosphate buffer (PB) to verify injection sites, and 15 mice (four
110 129S6/SvEvTac and 11 C57B/6J) were perfusion-fixed with glutaraldehyde (up to 2.5%) and formaldehyde (up
111 to 2%), followed by 20 mM glycine in cacodylate buffer to quench free aldehydes, to verify enzymatic activity of
112 mAPEX2 with Ni-DBA staining as described below.

114 **Histology and light microscopy**

115 For immunostaining, the fixed neurons were permeabilized with 0.2% Triton X-100 in PBS for 5 min,
116 rinsed in PBS, and blocked in 5% bovine serum albumin (BSA; Sigma-Aldrich) and 5% normal goat serum
117 (NGS; VectorLabs) for 15 min. The cells were then incubated overnight at 4°C with rabbit anti-myc (1:250;
118 Sigma-Aldrich Cat# C3956, RRID:AB_439680) in PBS with 2% BSA, 3% NGS, 0.1% Triton X-100, followed by

119 PBS washes and incubation for 1 hr with goat anti-rabbit IgG conjugated with Cy5 (1:100; Jackson
120 ImmunoResearch Labs Cat# 111-175-144, RRID:AB_2338013) in PBS with 2% BSA, 3% NGS, 0.1% Triton X-
121 100. After PBS washes, the coverslips containing neurons were mounted on glass microscope slides with
122 Aqua/Poly antifade mountant (PolyScience) for epifluorescence microscopy.

123 For DAB-labeling, the neurons were rinsed with cacodylate buffer and treated with 20 mM glycine. Then
124 the neurons were rinsed several times before being incubated with DAB (0.5 mg/ml) and H₂O₂ (0.03%) in
125 cacodylate buffer for 30 min. After buffer rinses, the coverslips were dehydrated in ethanol, cleared in xylenes,
126 and mounted on glass slides with DPX (Electron Microscopy Sciences) for brightfield microscopy.

127 To verify injection sites, the perfusion-fixed brain was vibratome-sectioned (100 µm thickness) for
128 epifluorescent microscopy to visualize GFP. To assess enzymatic activity of mAPEX2, the vibratome-sections
129 (50 µm thickness) of the fixed brain containing the dorsal hippocampus were incubated with Ni-DAB solution
130 (2.5 mM ammonium Ni [III] sulfate and 0.8 mM DAB in 0.1 M PB) for 20 min, before H₂O₂ (final concentration
131 0.0003%) was added and incubated for 10 min. After PB rinses, some of the Ni-DAB labeled sections were
132 processed for EM as described below. Otherwise, they were mounted on glass microscope slides, dehydrated
133 in ethanol, cleared with xylenes, and coverslips were applied with DPX. Epifluorescence and brightfield images
134 were acquired on a Zeiss Axio Imager.Z2 microscope with AxioCamMR3 camera, or a Zeiss Axio Imager.M2
135 with AxioCamHRc3 camera.

136 Instead of the TSA labeling (described below), some of the vibratome sections collected from fixed
137 hippocampal slices were permeabilized and blocked with PBS containing 0.3% Triton X-100, 1% BSA, and
138 10% NGS. The vibraslices were then incubated for overnight at RT with rabbit anti-HA antibody (1:1000; Cell
139 Signaling Technology Cat# 3724, RRID:AB_1549585), followed by 1 hr with the Cy5-conjugated goat anti-
140 rabbit IgG. After PBS rinses, the vibraslices were mounted on glass microscope slides and coverslips were
141 applied with Aqua/Poly mountant for imaging with a Leica TCS SP5 confocal microscope. Single channel
142 stacks (8 bit, 2048 × 2048 pixels at 19.1 or 28.6 nm/pixel) were acquired for GFP (458 nm laser) and Cy5 (633
143 nm laser) with 63× objective (oil, NA 1.32) at 4× zoom.

144

145 **Slice preparation, electrophysiology, optical stimulation**

146 Six weeks after rAAV injections, the mice were anesthetized deeply with isoflurane and then
147 decapitated. The brain was removed from the cranium, and the left hippocampus was dissected out and rinsed
148 with room temperature (RT) artificial cerebrospinal fluid (aCSF; pH = 7.4) containing (in mM) 117 NaCl, 5.3
149 KCl, 26 NaHCO₃, 1 NaH₂PO₄, 2.5 CaCl₂, 1.3 MgSO₄, and 10 D-glucose, and bubbled with 95% O₂-5% CO₂.
150 Slices (400 μm thickness; 4 per animal) from the dorsal hippocampus were cut at 70° transverse to the long
151 axis on a Stoelting tissue chopper and transferred in oxygenated aCSF to the supporting nets of interface
152 chambers in the Synchroslice system (Lohmann Research Equipment). The entire dissection and slice
153 preparation took ~5 min. This rapid dissection, together with the interface chamber design, provides for high-
154 quality ultrastructure during long acute slice experiments [24–27]. Hippocampal slices were placed on a net at
155 the liquid-gas interface between 30-31°C aCSF and humidified 95% O₂-5% CO₂ atmosphere bubbled through
156 35-36°C deionized water. For experiments in which the area CA3 was cut, the dissection was made using the
157 25-gauge needle on a 1-ml syringe after the slices were transferred into the chambers.

158 After 3 hr of incubation, the optical fiber (300 μm core diameter; 0.39 NA; ThorLabs FT300UMT) and
159 recording electrode (Thomas Recording) were positioned 400-600 μm apart in middle *stratum radiatum* of the
160 area CA1 with the fiber placed toward the area CA3. An optimal position of the recording electrode was chosen
161 by probing several points across CA1 and SR to achieve larger responses. One-ms pulses of laser ($\lambda = 473$
162 nm; maximal output ~14.5 mW as measured by a Thorlabs S130C light meter) were delivered from source
163 (ThorLabs S1FC473MM) controlled by a pulse generator (A.M.P. Instruments Master-8). The light meter
164 placed directly under the hippocampal slices showed approximately 30% loss of laser power through the slice
165 thickness, while the recording site was approximately 100 μm deep from the top surface. GluN receptors were
166 blocked by adding 4 μl of 25 mM d,l-2-amino-5-phosphonovaleric acid (APV; Abcam Cat# ab144498) to the 1
167 ml of aCSF in the interface recording chamber, which achieved an effective concentration of 50 μM d-APV.
168 Tetrodotoxin (TTX; final concentration 1 μM; Abcam Cat# ab120055) and 6,7-dinitroquinoxaline-2,3-dione
169 (DNQX; final concentration 20 μM; Abcam Cat# ab144496) were added to block voltage-gated sodium
170 channels and GluA receptors, respectively.

171 For electrical stimulation experiments, we replaced the optical fiber with a concentric bipolar electrode
172 (FHC, Inc.), which was used to deliver 200 μ s biphasic current pulses (100-300 μ A), lasting 100 μ s each for
173 positive and negative components of the stimulus. The initial eEPSP slope was \sim 50% of the maximal eEPSP
174 slope based on the input-output (IO) curve for each slice. IO curves were recorded by using a sequence of
175 pulses applied each 30 s with increasing stimulus intensity in 25 μ A increments. Test pulses were given at 1
176 pulse per 2.5 min unless stated otherwise, and eEPSP was recorded. Paired-pulse ratio (PPR) was measured
177 by applying two optical stimuli spaced 50-200 ms apart with 50 ms increment, every 30 s.

178

179 **Microwave-enhanced chemical fixation of hippocampal slices and TSA**

180 **labeling**

181 At end of recordings, the slices were immersed in fixative containing 1% glutaraldehyde and 4%
182 formaldehyde, and were microwaved immediately for 8-10 s at 700 W (modified from ref. 27). The fixed slices
183 were stored overnight at RT in the same fixative or in cacodylate buffer. After being immersed in 20 mM
184 glycine for 20 min and buffer rinses, the area CA1 was dissected out under a stereoscope with a microknife
185 and embedded into 9% agarose. Vibratome sections (50 μ m thickness) were then collected from the area of
186 optical stimulation to the location of the recording electrode. ChR2-GFP expression was confirmed with
187 epifluorescence microscopy. The sections were transferred to 0.1 M PB and then incubated with tyramide-
188 conjugated Alexa Fluor 647 (Thermo Fisher Scientific Cat# T20951) for 15 min in dark before H₂O₂ was added
189 (final concentration 0.0015%) and incubated for additional 10 min in dark. After washes with PB, the vibraslices
190 were washed in cacodylate buffer before being processed for 3DEM.

191

192 **Tissue processing for 3DEM**

193 TSA-labeled vibratome section was embedded into 9% agarose to protect it during the subsequent
194 processing, as described previously [28,29]. The tissue was immersed for 5 min in reduced osmium solution
195 containing 1% osmium tetroxide (OsO₄; Electron Microscopy Sciences) and 1.5% potassium ferrocyanide
196 (Sigma-Aldrich) in cacodylate buffer. After several buffer rinses, the tissue was immersed in 1% OsO₄ and two

197 cycles of microwave irradiation (175 W; 1 min on → 1 min off → 1 min on) were applied with cooling to ~15°C
198 in between. The tissue was rinsed in buffer several times, twice in purified water, and then immersed in 50%
199 ethanol before being dehydrated in ascending concentrations of ethanol (50%, 70%, 90%, 100%) containing
200 1% uranyl acetate (UA; Electron Microscopy Sciences) with application of microwave irradiation (250 W, 40 s
201 per ethanolic UA step). Ethanol was replaced by propylene oxide, and the tissue was infiltrated and embedded
202 into LX-112 resin (Ladd Research). Embedded tissue was trimmed under a stereomicroscope to expose the
203 region of interest containing the middle *stratum radiatum* of the area CA1. Serial thin sections (~60 nm
204 thickness) were cut with a diamond knife (Diatome Ultra35) on a ultramicrotome (Leica Ultracut UC6 or UC7)
205 and collected on Synpatek TEM grids (Be-Cu or gilded; Electron Microscopy Sciences or Ted Pella) coated
206 with film of polyetherimide (PEI; Goodfellow).

208 **Post-embedding immunogold labeling and gold enhancement**

209 Serial thin sections on gilded grids (4-6 sections per grid) were rinsed with Tris-buffered saline (TBS;
210 pH = 7.6) containing 0.01% Triton X-100 (TBS-T) and then blocked with 2% human serum albumin (HSA;
211 Sigma-Aldrich) and 10% NGS in TBS-T for 30 min. The sections were then incubated overnight at 4°C with
212 TBS-T containing 1% HSA, 1% NGS, and mouse anti-Cy5/Alexa Fluor 647 (cocktail of antibodies at 1:100
213 each from Sigma-Aldrich [Cat# C1117, RRID:AB_477654] and Miltenyi Biotec [custom-ordered antibody used
214 in their Anti-Cy5/Anti-Alexa Fluor 647 MicroBeads, Cat# 130-091-395]). After extensive washes with TBS-T
215 and TBS (pH = 8.2; TBS-8.2), the sections were incubated for 90 min at RT with TBS-8.2 containing 1% NGS,
216 0.5% polyethylene glycol, and goat anti-mouse antibody conjugated with colloidal gold (5 or 15 nm diameter;
217 BBI Solutions Cat# EM.GMHL5 or EM.GMHL15; 1:100). The sections were subsequently washed with TBS-8.2
218 containing additional 500 mM NaCl to reduce nonspecific antibody binding and then with TBS-8.2. The
219 sections labeled with 5 nm gold were further rinsed with purified water, incubated with gold enhancement
220 solution (GoldEnhance EM Plus; Nanoprobes) for 5 min at RT under ambient room light, and extensively
221 washed in purified water. Shortening the incubation time for gold enhancement should reduce formation of
222 background particles. All sections were stained with saturated aqueous solution of UA followed by lead citrate
223 [30] for 5 min each.

224

225 **Acquisition, alignment, and analysis of serial tSEM images**

226 Serial section images (8-bit TIFF; field size = 24,576 × 24,576 pixels) were acquired on a Zeiss
227 Supra40 field emission scanning electron microscope in transmission mode (tSEM) [31] with ATLAS package,
228 running at 28 kV, at 1.8 nm pixel size with 1.2 μs dwell time and 3.5 mm working distance. Serial tSEM images
229 were aligned automatically using Fiji [32] (RRID:SCR_002285; <http://fiji.sc>) with the TrakEM2 plugin [33]
230 (RRID:SCR_008954; <http://www.ini.uzh.ch/~acardona/trakem2.html>). The images were aligned rigidly first,
231 followed by application of elastic alignment [34]. The aligned image stack was cropped to 14,424 × 19,512
232 pixels (image field size = 912 μm²) with Fiji/TrakEM2 and imported into Reconstruct [35] (RRID:SCR_002716;
233 <http://synapseweb.clm.utexas.edu/software-0>) for 3D reconstruction and analyses. An image of grating replica
234 (Electron Microscopy Sciences Cat# 80051), acquired along with serial section images, was used to calibrate
235 pixel size. Mean section thickness was estimated based on the diameter of longitudinally sectioned
236 mitochondria [36]. In serial tSEM images of sections that were immunolabeled, we first identified all axons
237 containing any gold particles. An axon was considered as positively labeled if it contained gold particles (> 10
238 nm diameter after gold enhancement) outside mitochondria in at least two of three serial sections. To measure
239 the density of enhanced gold particles, all particles were counted in four immunolabeled sections and
240 categorized as positive labels or background. Particle densities were calculated from these counts divided by
241 their respective areas in each of the analyzed sections. The density of axonal boutons was calculated based
242 on the unbiased volume method [37], in which all boutons that did not intersect the exclusion planes were
243 counted in a sub-volume of the 3DEM series encompassing 8 × 8 × 4.1 μm.

244

245 **Control for immunogold labeling**

246 To control for non-specific binding of the primary and secondary antibodies, we collected serial thin
247 sections from rAAV-injected tissue that was not labeled with tyramide-conjugated dye, but otherwise
248 underwent immunogold labeling. This tissue was derived from the same slice as the one used for 3D
249 reconstruction of a labeled axon as described above. In three consecutive sections (image field size = 1,520

250 μm^2) from this control series, we counted axons containing at least one enhanced gold particle (> 10 nm
251 diameter). None of these axons qualified as positively labeled, indicating the false positive rate is negligible.

252 An additional control was performed for non-specific antibody binding, in which another set of serial thin
253 sections from rAAV-injected, tyramide-labeled tissue underwent immunogold labeling with the primary antibody
254 omitted. These sections also showed no axons that qualified as positively labeled in the EM images. To control
255 for self-nucleation of gold enhancement reagent, a tSEM image was also acquired from serial thin sections of
256 the area CA1 that were not immunolabeled, but were incubated with the gold enhancement reagent as above
257 and then stained with UA and lead citrate.

258 To measure the size of enhanced gold particles, the antibody conjugated with 5 nm gold was blotted on
259 a PEI-coated TEM grid and then treated with the gold enhancement reagent as above. We acquired a tSEM
260 image from a square field encompassing 4,096 pixels per side at 1.8 nm/pixel and thresholded the image to
261 identify a total of 527 particles for their size measurement with the particle analysis function of Fiji. This
262 measures the maximum caliper, which is the longest distance between any two points along the selection
263 boundary. Enhanced particles that obviously formed from two or more 5 nm particles placed in close proximity,
264 as evidenced by the presence of negative curvatures, were excluded from this analysis.

266 **Confocal image analysis**

267 Fiji was used for processing and analysis of the confocal images. Maximum intensity projection images
268 were generated from 5 optical sections encompassing $51.5 \times 34.3 \times 3.2 \mu\text{m}$ in x, y, and z. Image stacks from
269 Cy5 channel were corrected for bleaching (the simple ratio method under bleach correction function in Fiji)
270 before they were projected. Projected images from GFP and Cy5 channels were merged and thresholded to
271 identify all puncta (≥ 100 nm diameter) labeled with either of the fluorophores, which were then assessed for
272 co-expression in single channel images. A total of 682 labeled puncta were identified, excluding those at edges
273 of the image. Acquisition of single channel image stacks for each of the fluorophores, rather than dual-channel
274 stacks, caused a slight mismatch in their z-positions, which may have contributed to a small fraction of puncta
275 to appear as single-labeled. The density of GFP-positive puncta was calculated from three additional confocal

276 image stacks, encompassing $39.1 \times 39.1 \times 4.4 \mu\text{m}$ (two image stacks) or $58.6 \times 58.6 \times 3.2 \mu\text{m}$ (one image
277 stack).

279 **Analysis of physiology recordings**

280 The initial acquisition and analysis of EPSP were performed with SynchroBrain software (Lohmann
281 Research Equipment). The initial maximum slope was measured over a 0.2-0.8 ms time frame that was held
282 constant for all recordings in each slice. To calculate the magnitude of LTP, EPSP slopes were normalized to
283 the average slopes obtained during the last 30 min of baseline recordings before the delivery of the first HFS.
284 Then values across slices (mean \pm SEM) were presented as times baseline. LTP magnitude at 30, 60, 120,
285 and 180 min post-HFS was calculated by averaging the values for the preceding 20 min. Prism software
286 package (Graphpad Software) was used for statistical analysis and plotting. The main tests performed were
287 Student's t-test and analysis of variance (ANOVA). Specific statistical tests and results are shown in the
288 corresponding figure captions.

290 **Data availability**

291 The following files generated and analyzed during the current study are deposited at Texas Data Repository
292 (doi:10.18738/T8/QP43LB):

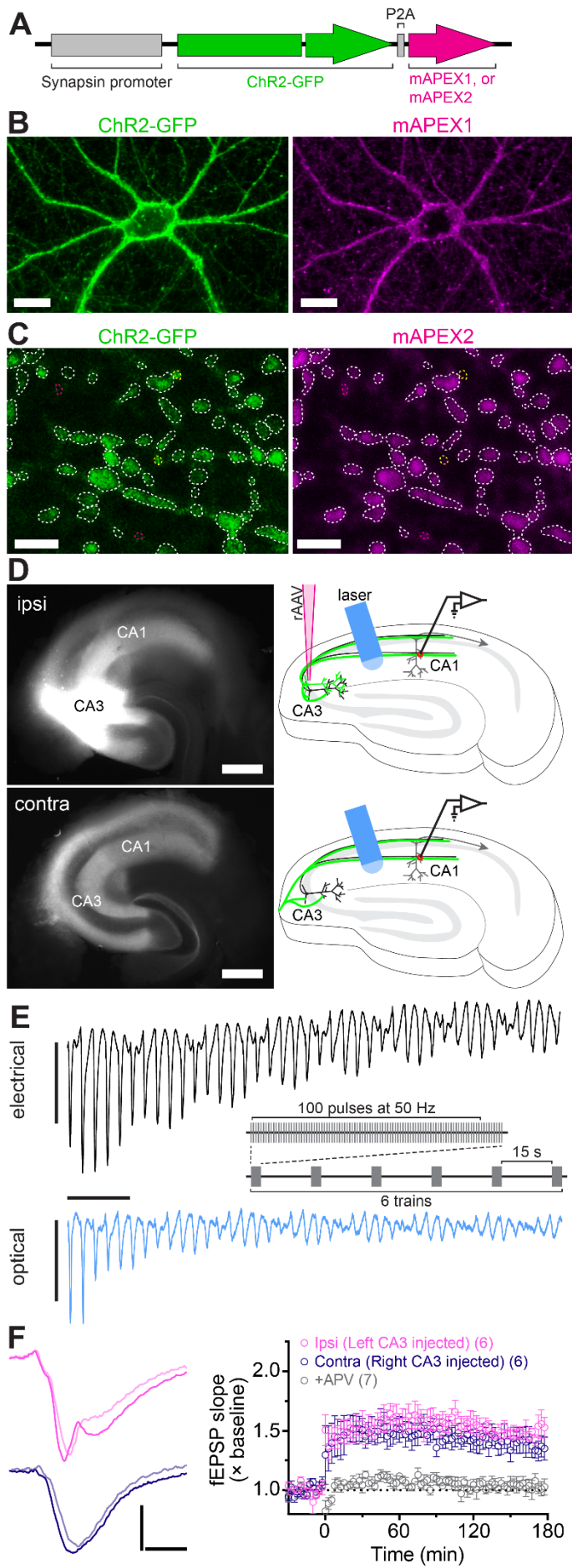
- 293 1. The original, unaligned serial tSEM images (VYLNH_raw1.zip [11.1 GB], VYLNH_raw2.zip [11.4 GB],
294 and VYLNH_raw3.zip [12.0 GB])
- 295 2. The aligned 3DEM dataset (VYLNH_20181017.zip; 14.8 GB)
- 296 3. S1 Video (S1_video.mp4; 71.1 MB).

299 **Results**

300 **Potentiation of synapses using light**

301 We designed an adeno-associated virus vector (rAAV) for stimulating and tracking individual neurons
302 and the trajectories of their axons. The construct encoded two proteins: a ChR2 [14] fused to GFP [15] and an
303 APX from *P. sativum* [17] to generate the electron-dense deposits detected in EM. We chose ChR2^{ET/TC} based
304 on its conductance and ability to sustain optical stimulation up to 60 Hz [14]. We modified APX to include
305 amino acid substitutions for increased stability and enzymatic activity [5,6]. We enhanced its membrane and
306 synapse targeting by adding a palmitoylation signal from growth-associated protein 43 (GAP-43) [18] to
307 produce mAPEX2 (Fig 1A). A virus encoding ChR2 and mAPEX2 ensured that both proteins co-localized in the
308 same cells. The observations from dissociated neurons and acute hippocampal slices reflect ChR2-GFP and
309 mAPEX2 co-expression at the cellular and synaptic levels (Figs 1B and 1C).

310



312 **Fig 1. Viral expression of ChR2-GFP and mAPEX, and induction of optical L-LTP.** (A) The rAAV was
313 designed to co-express ChR2-GFP and mAPEX under a single synapsin promoter in neurons. During
314 translation, the P2A peptide self-cleaves to yield the two proteins. (B) Cultured hippocampal neurons infected
315 with the rAAV co-expressed ChR2-GFP and mAPEX1. Scale bars = 25 μ m. (C) ChR2-GFP was co-expressed
316 with mAPEX2 in the same axons in the area CA1 (dotted white lines). Yellow and magenta lines indicate
317 ChR2-GFP only and mAPEX2 only puncta, respectively. Scale bars = 2 μ m. (D) GFP fluorescence images
318 (left) and experimental configurations (right) in ipsilateral (top, ipsi) and contralateral (bottom, contra)
319 hippocampal slices. Scale bars = 500 μ m. (E) Electrical (top) and optical (bottom) EPSPs evoked by a train of
320 50 Hz stimulations, recorded from CA1 middle *stratum radiatum* (C57B/6J strain). Responses to the first 40
321 pulses are shown and the stimulation artifacts are clipped from the eEPSP data. The inset shows HFS protocol
322 for LTP induction. Scale bars = 1 ms, 2 mV (electrical), 1 mV (optical). (F) Optical HFS induced L-LTP in the
323 Schaffer collateral and commissural pathways. *Left*: Representative oEPSP traces from ipsilateral (top) and
324 contralateral (bottom) slices before (light shaded line) and 3 hr after (solid line) HFS. *Right*: Time course of
325 oEPSP slope (mean \pm SEM) showing optical L-LTP in ipsilateral (pink) and contralateral (purple) slices.
326 Addition of APV blocked L-LTP (grey). The number of slices is indicated in parentheses. Scale bars = 4 ms, 1
327 mV.

328
329
330 We injected the rAAV vector into *stratum pyramidale* of the hippocampal area CA3 in one hemisphere
331 of the adult mouse brain (S1 Fig, A). Epifluorescence microscopy confirmed robust expression of ChR2-GFP in
332 the CA3 neurons and in Schaffer collaterals extending into ipsilateral area CA1. The contralateral hippocampus
333 showed GFP-labeled commissural/associational fibers in the areas CA1 and CA3 (S1 Fig, B).

334 Four to six weeks after virus injection we prepared acute transverse slices from ipsilateral or
335 contralateral hippocampus, four per hemisphere, covering the dorsal region. The slices were allowed to
336 recover for 3 hr in interface chambers [38]. We then applied pulses of blue light (473 nm wavelength; ~14.5
337 mW power) via an optical fiber (300 μ m diameter) positioned over the area CA1 *stratum radiatum* in each
338 chamber (Fig 1D) and examined the ChR2 responses. Typically, 2-4 slices displayed optical responses. In

339 these slices, optically-evoked field excitatory postsynaptic potentials (oEPSP) and population spike shapes
340 recorded within different strata of area CA1 resembled the waveforms observed previously with electrical
341 stimulation (eEPSP) [39–41], confirming a similar propagation of the signal. Although oEPSP were similar to
342 eEPSP, we noticed a difference in the shape of the waveform: the initial activation stage consisted of more
343 than one component, visible as change in slope. We assume this could be due to asynchrony of fiber firing at
344 different sites along *stratum radiatum* because of the relatively larger area stimulated by light compared to
345 concentric bipolar stimulating electrodes. In accordance with prior reports, oEPSP had comparable slopes and
346 amplitudes between ipsilateral and contralateral groups of fibers [11,42], although these parameters were
347 significantly smaller than in electrical responses (S1 Fig, D). Light-evoked short-term plasticity [43], measured
348 as paired-pulse ratio (PPR), was also detected (S1 Fig, E). Optical responses were blocked by TTX (S1 Fig, F)
349 and DNQX (S1 Fig, F), demonstrating their dependence on voltage-gated sodium channels and GluA
350 receptors, respectively.

351 Next, we confirmed that ChR2 could follow trains of light pulses needed to induce L-LTP. Stimuli were
352 delivered at 50 Hz (Fig 1E), a frequency sufficient for LTP induction [10,44] that also allows more time for
353 ChR2 to recover between stimulation episodes [14] than the higher frequencies (100 Hz or higher, including
354 theta-burst) typically used for electrical induction of LTP. Optical stimulation resulted in the trains of evoked
355 oEPSP in CA1 *stratum radiatum* (Fig 1E, bottom) in a pattern comparable to the one evoked by 50 Hz
356 electrical stimulation (Fig 1E, top). However, optical responses exhibited smaller initial amplitudes and
357 underwent stronger desensitization during the trains of light stimuli.

358 Smaller amplitudes in our optical experiments could be due to incomplete ChR2 activation or to the
359 presence of ChR2 in a relatively small subset of axons. To differentiate between these possibilities, we
360 recorded oEPSP under varied light stimulus intensity. Input-output curves of oEPSP slope as a function of light
361 intensity showed an apparent saturation at maximum level of ~14.5 mW (S2 Fig). Thus, our optical stimulation
362 protocol maximized activation of all the targeted axons.

363 Optical stimulus regimes produced L-LTP that lasted for at least 3 hr (Fig 1F). Optically stimulated
364 ipsilateral and contralateral slices showed the same degree of potentiation. However, the likelihood of
365 achieving L-LTP varied, and the success rate was 67% and 42% for ipsilateral and contralateral slices,

366 respectively. Optical L-LTP induction was blocked by application of 2-amino-5-phosphonovaleric acid (APV),
367 reflecting a dependence on GluN receptors (Fig 1F).

368 To isolate the rAAV-targeted CA3 axons as the sole source of excitatory synaptic transmission and to
369 avoid possible recruitment of unlabeled fibers, we recorded oEPSP from contralateral slices with the area CA3
370 severed pre-recovery (Fig 2A). Using contralateral slices additionally eliminated the likelihood that CA1
371 neurons could be labeled with Chr2 and stimulated independently of the CA3 axons. Severing CA3 had little
372 effect on the likelihood or magnitude of L-LTP from electrical stimulation (Fig 2B). In contrast, the induction rate
373 was reduced from 42% to 33% in contralateral sections with severed CA3, and the magnitude of LTP was
374 smaller at 1 hr compared to intact sections, but nearly identical by 3 hr (Figs 2C and 2D). The magnitude of
375 electrical LTP in intact and cut slices was similar at 1 hr and 3 hr post-stimulation (Figs 2B and 2D). We
376 conclude that the optical stimulation of genetically specified CA3 commissural fibers is sufficient to induce L-
377 LTP in the area CA1.

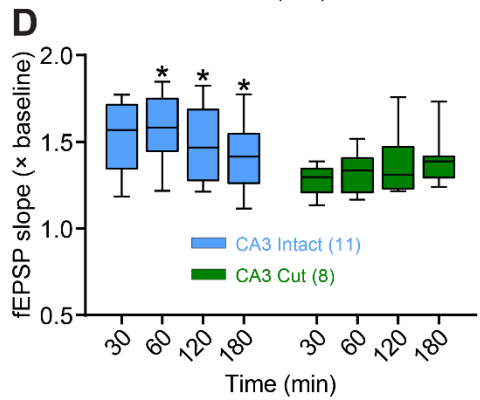
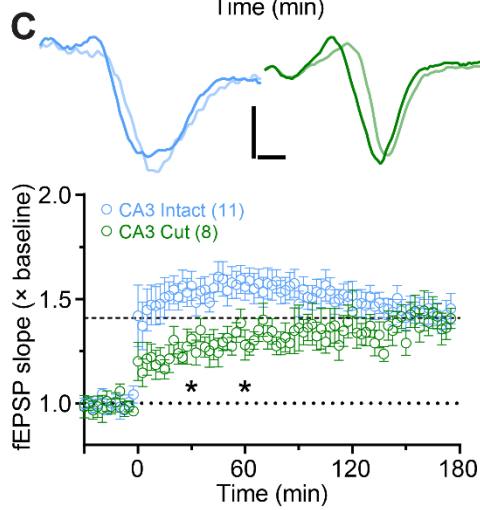
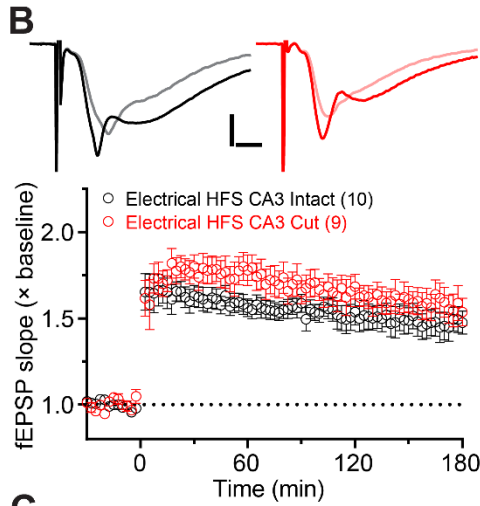
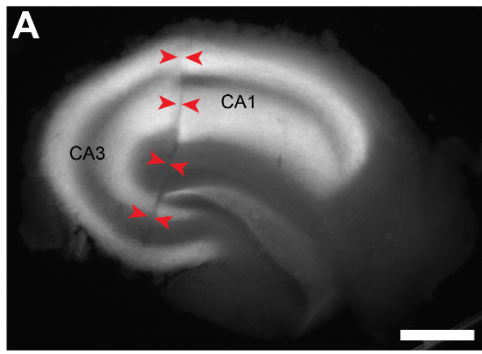
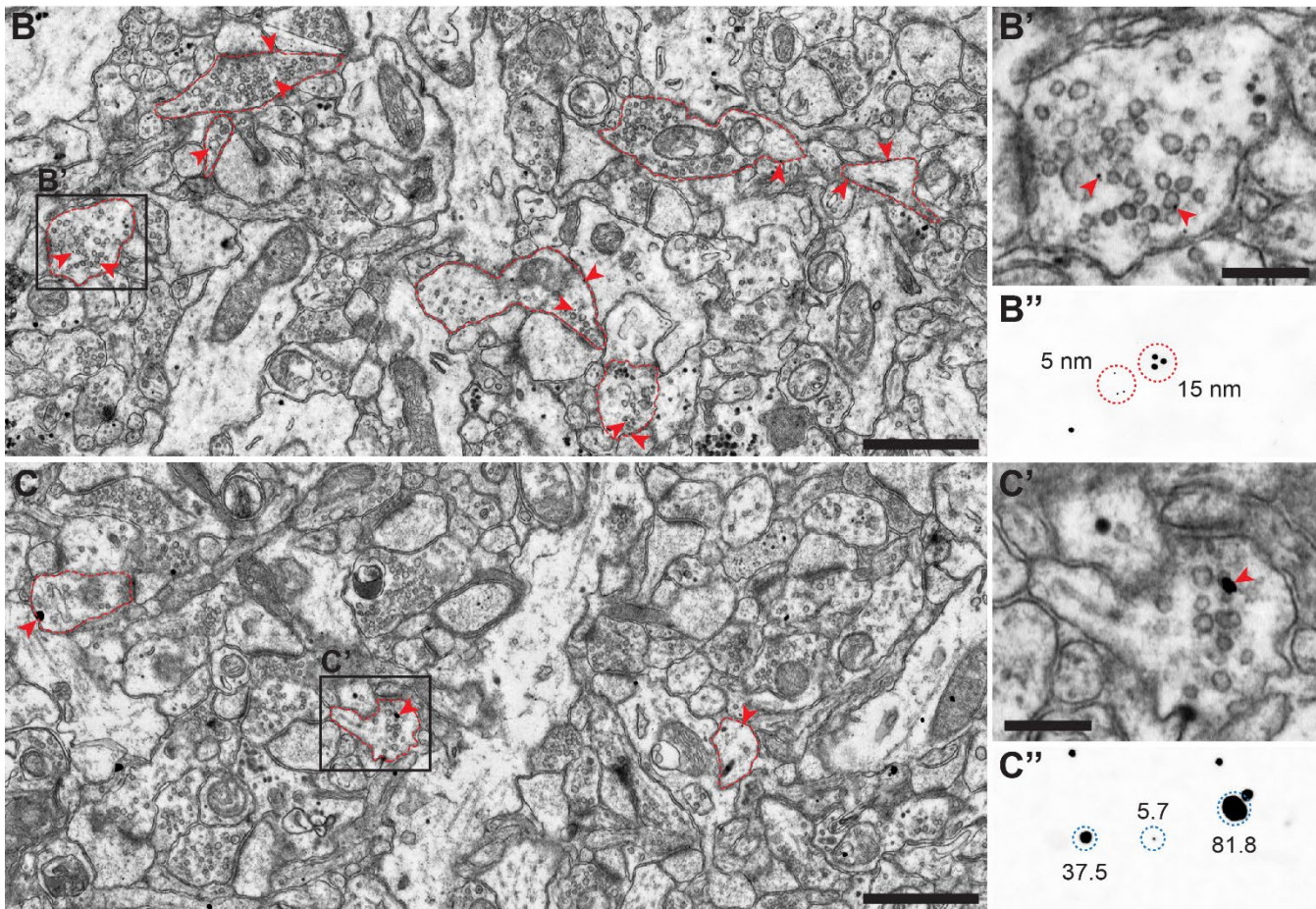
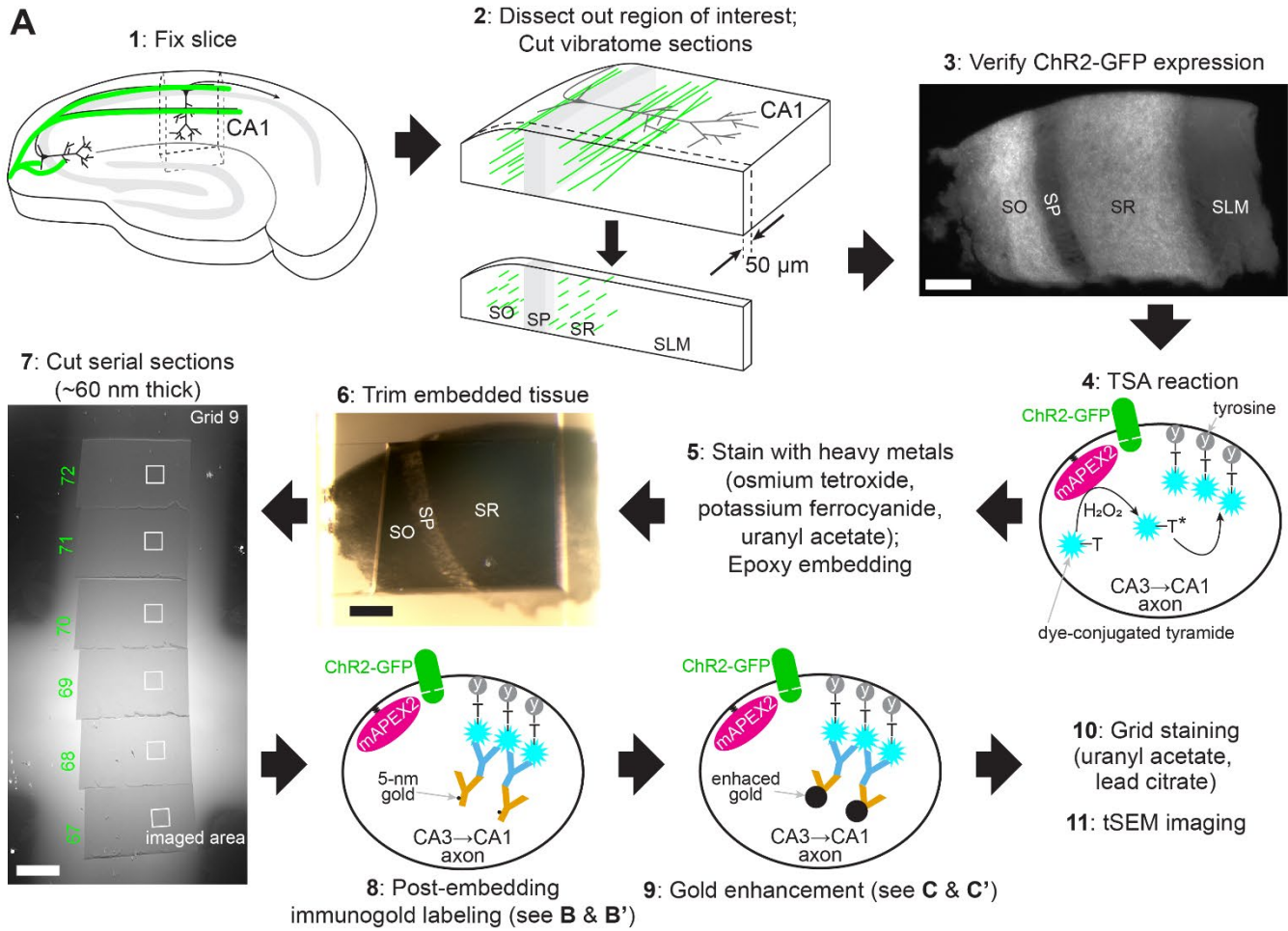


Fig 2. Optical stimulation of CA3→CA1 commissural fibers was sufficient for L-LTP. (A) Representative image of a contralateral slice with CA3 cut off from CA1. Scale bar = 500 μm . (B-C). LTP induced by electrical (B) and optical (C) HFS in intact and cut slices. The example traces show EPSPs recorded before (light shaded lines) and 3 hr after HFS (solid lines). Optical LTP magnitude (C) at 30 and 60 min post-HFS was significantly different between intact and cut slices (oEPSP slope $F_{(1, 17)} = 4.74$, $p < 0.05$; Time $F_{(3, 51)} = 0.95$, $p > 0.05$; Interaction $F_{(3, 51)} = 6.60$, $p < 0.0001$; repeated measures two-way ANOVA with Bonferroni's post-hoc tests). Scale bars = 2 ms, 2 mV (B); 1 ms, 0.5 mV (C). (D) Summary data for oEPSP slope change at different time points following optical HFS in intact and cut slices. The intact slices showed significant changes in LTP magnitude in the last 120 min of recordings ($F_{(1.28, 12.8)} = 5.75$, $p < 0.05$; repeated measures one-way ANOVA). The box plots show medians and interquartile ranges, with whiskers extending from minimum to maximum values. The number of slices used for each condition is indicated in parentheses.

Post hoc labeling and reconstruction of potentiated synapses

Post hoc 3DEM analysis of activated synapses and subcellular organelles requires well-preserved slice tissue, which is typically achieved by chemical fixation with glutaraldehyde. Thus, the expressed EM tag must retain its enzymatic activity to produce electron-dense deposits in fixed samples. Like the original APEX [5,6], we verified that mAPEX2 was active after glutaraldehyde fixation by observing conversion of 3,3'-diaminobenzidine (DAB) into osmiophilic polymers, which appear dark brown under light microscopy or as amorphous electron-dense deposits under EM (S3 Fig).

We fixed brain slices that displayed L-LTP following optical stimulation at the 3 hr time point and had robust GFP labeling (Fig 3A, Step 1; see Materials and Methods). Orthogonal vibratome sections spanning area CA1 (Fig 3A, Steps 2-3) were incubated with tyramide conjugated with Alexa Fluor 647. Membrane-associated mAPEX2 then catalyzed the tyramide signal amplification reaction (TSA) locally upon the addition of H_2O_2 (Fig 3A, Step 4). After heavy metal staining and epoxy embedding, serial thin sections (~60 nm thickness) were collected from a region of interest containing the middle of *stratum radiatum* (Fig 3A, Steps 5-7). For the series shown in Figs 3A (Step 7), 3C, and 4, a total of 72 sections were collected from portions of tissue at least 10 μm from the surface of a 50 μm thick vibratome section.



409 **Fig 3. mAPEX2-catalyzed labeling and 3DEM identification of rAAV-targeted axons. (A)** Workflow for
410 processing of hippocampal slices following optical L-LTP. Vibratome sections from the fixed area CA1
411 underwent tyramide signal amplification (TSA) catalyzed by mAPEX2 to deposit Alexa Fluor dye in the targeted
412 axons. The dye-labeled section was then stained with heavy metals and embedded into epoxy before being cut
413 into serial thin sections. The dye-containing axons in a subset of the sections were immunolabeled with 5 nm
414 gold particles, followed by gold enhancement. Scale bars = 100 μ m. **(B and B')** A low magnification tSEM
415 image of the area CA1 *stratum radiatum* after immunolabeling (Step 8 in **A**). Axonal boutons indicated by red
416 contours were positively labeled with 5 nm gold particles (red arrowheads). Area indicated by black rectangle is
417 enlarged in **B'**. Scale bar = 1 μ m in **B**, 250 nm in **B'**. **(B'')** A tSEM image of colloidal gold particles (5 nm and
418 15 nm). To visualize the 5 nm particles more clearly, this image was acquired at 1 nm/pixel and scaled to the
419 same magnification as **B'**. **(C and C')** Same as **B and B'**, imaged after gold enhancement (Step 9 in **A**). Scale
420 bar = 1 μ m in **C**, 250 nm in **C'**. **(C'')** A tSEM image of enhanced gold particles. The numbers indicate diameters
421 in nm (also see S5 Fig 5).

422
423 In a subset of sections, at the beginning and end of the series, we labeled the axons expressing
424 mAPEX2 that now contained the dye-tyramide molecules with anti-dye antibodies, then gold-conjugated
425 secondary antibodies (Fig 3A, Step 8). This limited labeling ensured that the ultrastructure was visible while
426 having sufficient labeling to identify the genetically-targeted axons unambiguously (Figs 3B and 3B'). We
427 considered an axon to be positively labeled if it contained gold particles in at least two of three serial sections
428 per grid. We tested 5 nm and 15 nm colloidal gold particles. Staining with smaller particles suffered from
429 relatively low signal-to-noise, limited visibility of the gold particles (nominal particle size = 5 nm vs. pixel size =
430 1.8-2.0 nm), and difficulty in distinguishing the particles from artifacts and subcellular features of similar size
431 (Fig 3B' and S4 Fig). Working with 15 nm gold particles improved particle visibility (Fig 3B'') but reduced
432 labeling sensitivity, making labeled axons harder to identify. We boosted the visibility of 5 nm particles by
433 increasing their size with a gold enhancement technique [45] (Fig 3A, Step 9). The enhanced particles were of
434 high contrast and uniformly electron-dense with smooth edges, which made them distinct from artifacts and
435 subcellular structures of similar size (e.g., glycogen granules, darkly stained membrane, and precipitation from

436 post-section staining; Figs 3C, 3C', and S4 Fig). Enhancement of immunogold particles blotted on a blank grid
437 resulted in particles with diameter ranging from 2.5 nm to 85.3 nm (median = 37.1 nm), significantly improving
438 their ease of identification (Fig 3C'' and S5 Fig). Control sections devoid of immunogold labeling, but treated
439 with the enhancement reagent, showed electron-dense particles with the diameter ≤ 10 nm, likely resulting
440 from reagent self-nucleation (S5 Fig). We therefore excluded these small particles during identification of
441 labeled axons. Thus, in the gold enhanced material, our criterion for positively labeled axons was the presence
442 of particles > 10 nm in diameter in at least two of three consecutive sections.

443 In this 3DEM series, 23 axons (2 axons per $100 \mu\text{m}^2$) were positively labeled, and 170 axons (19 axons
444 per $100 \mu\text{m}^2$) contained enhanced gold particles but did not meet the criteria. The 23 axons that were
445 confirmed positive could include true and false positives, while the 170 negative axons would reflect true and
446 false negatives. To estimate the numbers in each category, we performed control immunogold labeling on
447 serial thin sections from the same rAAV-injected tissue that otherwise did not undergo labeling with the
448 tyramide-conjugated dye. In these sections, we found 223 axons containing at least one enhanced gold
449 particle (15 axons per $100 \mu\text{m}^2$). None of these axons qualified as positively labeled, indicating that the false
450 positive rate is negligible. Thus, we deemed as true negatives the 15 of 19 axons per $100 \mu\text{m}^2$ that did not
451 meet the criteria in the tyramide-labeled series. This suggests that the remaining 4 of 19 axons could be false
452 negatives under our current labeling protocol for 3DEM, and that positively labeled axons could represent
453 $\sim 30\%$ (2 positively labeled out of 6 containing gold particles) of rAAV targeted axons.

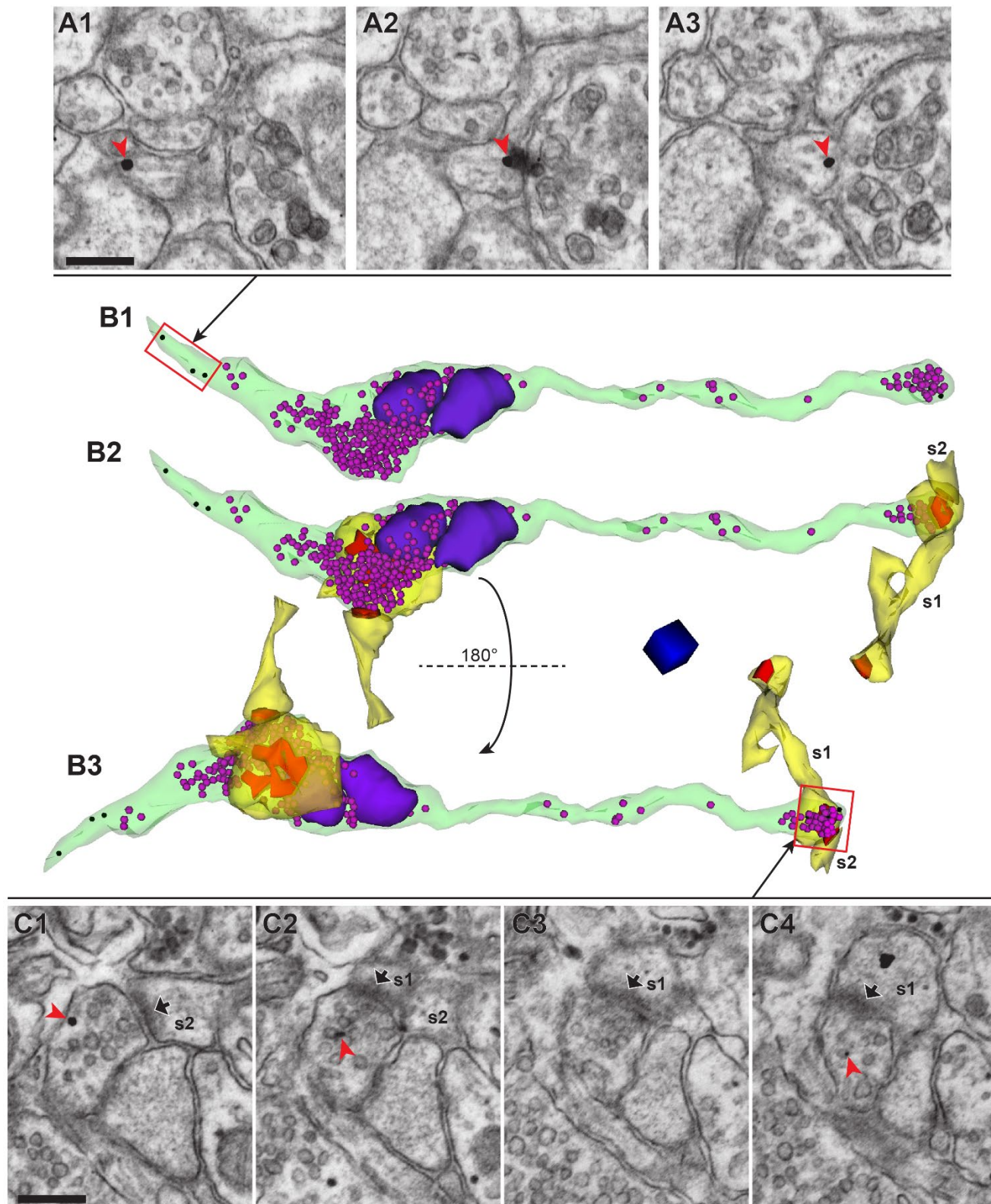
454 We also measured the density of boutons belonging to positively labeled axons in the 3DEM series (12
455 per $1,000 \mu\text{m}^3$), and that of GFP-positive puncta in three confocal image volumes (mean = 35 per $1,000 \mu\text{m}^3$;
456 range = 20 to 47 per $1,000 \mu\text{m}^3$). Although measured from tissue samples from different animals, these
457 observations also suggest that the confirmed positives could represent $\sim 30\%$ of the rAAV targeted axons.
458 However, frequency of potential false negatives relative to the total number of axonal boutons is small ($\sim 1\%$, or
459 about 10-30 of 2604 boutons per $1,000 \mu\text{m}^3$). It will be possible to uncover ultrastructural correlates of
460 potentiation by comparing labeled axons from slices that have and have not received optical stimulations. To
461 show that the plasticity-related ultrastructural changes are restricted to the positively labeled axons, one could

462 also analyze unlabeled axons from slices with or without optical stimulations. In this case, the contribution of
463 false negatives to the pool of unlabeled axons in either preparation will be extremely low, on the order of 1%.

464 The density of positive particles within labeled axons after gold enhancement was 2.85 ± 0.88 per μm^2 ,
465 while the overall background particle density was 0.33 ± 0.02 per μm^2 (mean \pm SEM; $n = 4$ sections). Thus, the
466 signal-to noise ratio was 8.7.

467 Finally, we reconstructed a labeled axon from an rAAV-infected CA3 neuron forming synapses onto
468 dendritic spines in middle *stratum radiatum* of the area CA1 from a slice that showed optically induced L-LTP
469 (Fig 4 and S1 Video). This axon contained gold particles in the first three sections and three of the last four
470 sections that were immunolabeled (Figs 4A and 4C). This axon had two multi-synaptic boutons, one of which
471 was reconstructed only partially because it was at one edge of the serial section series (Fig 4B). This partial
472 bouton formed synapses with two spines (s1 and s2 in Fig 4B; also see S1 Video). One of these spines (s1)
473 had another branch that formed a synapse with a separate axonal bouton that was unlabeled. The synapses
474 on the branched spine (s1) were both macular and of similar sizes ($0.029 \mu\text{m}^2$ and $0.021 \mu\text{m}^2$). The bouton that
475 was completely reconstructed contained two mitochondria and formed synapses with two spines from different
476 dendrites (Fig 4B; S1 Video). One of these synapses was perforated (area = $0.11 \mu\text{m}^2$), while the other was
477 macular (area = $0.037 \mu\text{m}^2$). These findings are consistent with synapses on this axon having been potentiated
478 [46].

479



480
481 **Fig 4. Post-embedding immunogold labeling for Alexa Fluor dyes deposited by mAPEX2-driven TSA**
482 **reaction allowed for 3DEM identification of rAAV-targeted axons, while maintaining excellent**
483 **ultrastructure. (A1-A3) Three adjacent serial tSEM images of an axon containing immunogold labeling (red**

484 arrowhead). Scale bar = 250 nm. **(B1)** 3D reconstruction of the labeled axon (green) shown in **A**, which
485 contained immunogold labels (black spheres) and synaptic vesicles (magenta spheres). Two mitochondria
486 (purple) were associated with one of the two boutons. Red rectangle represents a portion of this axon shown in
487 **A1-A3**. **(B2)** Same axon as **B1**, with reconstructions of spines (yellow) forming synapses (red) with this axon.
488 Note, s1 was a branched spine with one of the heads forming a synapse with another axon. The second spine
489 (s2) and its PSD could be reconstructed only partially because they were located at the end of the tSEM image
490 series. Both axonal boutons are multi-synaptic, with each bouton forming synapses with two spines originating
491 from different dendrites. **(B3)** Same as **B2**, rotated along the horizontal axis 180° to provide a different view of
492 synapses and spines. One of the synapses at mitochondria-containing bouton was perforated (also see S1
493 Video). Red rectangle represents a portion of this axonal bouton shown in **C1-C4**. Scale cube = 250 nm per
494 side. **(C1-C4)** Four adjacent serial tSEM images of the gold-labeled (red arrowhead) axonal bouton, forming
495 synapses with two dendritic spines (s1 and s2; PSDs indicated by black arrows). Scale bar = 250 nm.

497 Discussion

498 Genetic targeting of specific neuron populations for imaging and activation has transformed structure-
499 function studies of brain circuitry. Until now, however, tools for examining the ultrastructure of genetically
500 specified neurons post-manipulation have been lacking. Here we describe methods for inducing activity-
501 dependent plasticity in a genetically defined subset of neuronal synapses and for identifying optogenetically
502 potentiated axons. We demonstrate light-evoked L-LTP in acute hippocampal slices. Previous ultrastructural
503 studies of potentiated synapses examined effects across differentially activated populations of synapses, but
504 the histories of individual synapses were unknown. The unilateral infection of CA3 neurons yields CA3→CA1
505 projections that co-express a light-dependent actuator and an EM tag from a single rAAV amid a larger
506 population of unlabeled axons. Hence the advance of our approach is that recently potentiated synapses can
507 be compared to neighboring unstimulated synapses in the same block of tissue.

Light stimulation of CA3 axons resulted in robust oEPSP in ChR2-expressing hippocampal slices

In hippocampal slices prepared from rAAV injected animals, light pulses induced oEPSP that depended on voltage-gated sodium channels and GluA receptors. The light intensity used for optical high-frequency stimulation (HFS) was shown to achieve the maximal responses. Furthermore, the expressed ChR2 reliably responded to light trains delivered at 50 Hz, a frequency sufficient to produce L-LTP [10,44]. Together these findings ensure that synapses identified by the *post hoc* 3DEM analysis were activated during the optogenetic LTP induction protocol.

Optical L-LTP was produced in intact hippocampal slices expressing ChR2-GFP and mAPEX2

We used high-frequency optical stimulation to induce GluN receptor-dependent L-LTP lasting at least 3 hr in a subpopulation of CA3→CA1 synapses containing presynaptically expressed ChR2. Recent reports suggest molecular and synaptic asymmetry between right and left hippocampus affecting LTP induction and endurance [11,47]. These findings prompted us to explore induction and expression of optical L-LTP in both hemispheres. The rAAV was injected into the left (ipsilateral) or right (contralateral) hippocampus, and all slices were prepared from the left hemisphere. L-LTP reached similar magnitudes whether the ipsilateral Schaffer collaterals or contralateral commissural axons were optically stimulated.

This discrepancy with the prior papers could be due to technical differences, including recording configurations (field vs. single-cell recordings) or plane of hippocampal slices (transverse vs. coronal). Our findings are also consistent with prior studies using electrical stimulation. For example, in rat hippocampal slices where Schaffer collaterals or commissural fibers were isolated by kainic acid lesion, the properties of LTP produced independently by each pathway were similar to those observed in unlesioned slices [42,48]. Recent *in vivo* studies with intact brain also detected a robust LTP mediated by Schaffer or commissural axons [49].

Optical L-LTP did not require recruitment of unlabeled axons

In order to make direct comparisons between synapses with different activation histories, optical HFS must activate only the rAAV-targeted axons. In the intact contralateral system, the measured oEPSP responses could be contaminated if back-propagating action potentials from labeled commissural fibers were to recruit neighboring unlabeled CA3 neurons through recurrent collaterals. To test whether our oEPSP responses had been amplified through light-independent intra-hippocampal connections, we compared optical stimulation in contralateral slices with intact or severed area CA3. Compared to intact slices, the cut slices had a lower success rate for L-LTP (42% vs. 33%), yet these results suggest L-LTP could certainly be achieved without recruitment of unlabeled axons.

There was a slower rise to maximum LTP magnitude in the cut slices that might have been caused by reduced synchronicity of firing if unlabeled axons are recruited in the intact system. Other experiments have witnessed this slow rise to LTP. For example, LTP can be produced with a slow onset with frequencies normally used for induction of LTD (1-5 Hz) [50]. Sometimes weak presynaptic stimulation paired with depolarization of postsynaptic neurons results in LTP with a similar slow rise early during expression [51,52]. Induction of mGluR-dependent [53] or BDNF-dependent LTP [54] both show slow rises in LTP magnitude. Furthermore, at the developmental onset of L-LTP the expression can also have a slow rise [38]. Each of these conditions is also submaximal in the induction paradigms, not unlike activation of less than all the axons with light versus electrical stimulation. However, since both intact and cut slices expressed optically induced L-LTP of the same magnitude at 2 and 3 hr post induction, the recruitment of unlabeled axons was unlikely to be the critical factor.

mAPEX2 labeled axons are compatible with ultrastructural analysis of synapses

To study synaptic connectivity and function, it is necessary to know which synapses were engaged. This level of analysis has been limited by the availability of ultrastructural tools to identify activated synapses. We aimed to label the targeted axons discretely without obscuring or compromising the integrity of their

561 subcellular and synaptic components. Since the genetically encoded mAPEX2 was expressed in the tissue and
562 compatible with microwave-enhanced chemical fixation containing glutaraldehyde, it replaced the use of pre-
563 embedding antibody labeling to identify rAAV-targeted axons. mAPEX2 accommodates tyramide-conjugated
564 fluorescent dyes, which are then deposited in the targeted cells by the TSA reaction [55]. The combination of
565 mAPEX2-driven TSA reaction and post-embedding immunogold labeling allowed reliable identification of the
566 targeted cells throughout the 50 μm vibraslices, at depths not accessible by pre-embedding antibody methods
567 ($< 10 \mu\text{m}$). These features revealed optimal preservation of ultrastructure in acute slice tissue for analyses of
568 synapses and organelles after targeted optogenetic manipulations. We show that this process is compatible
569 with conventional fixation, processing, epoxy infiltration, and post-embedding immunogold labeling [56,57]. We
570 show that only a subset of serial sections need be labeled to track axons from the targeted cells, and even in
571 the labeled sections, the particles did not obscure objects of interest.

572 L-LTP induced by electrical theta-burst stimulation in the area CA1 is associated with an increase in the
573 abundance of multi-synaptic boutons in the population of stimulated axons [46]. The 3D reconstruction of a
574 labeled axon from an optogenetically potentiated slice showed two neighboring multi-synaptic boutons,
575 consistent with this prior report, but now from an identified axon. Future work will address whether such shifts
576 in synapse configurations are dependent on activation history.

577 The methods described here provide reliable physiology and labeling compatible with conventional
578 tissue fixation and the processing techniques needed to preserve subcellular organelles. They make an ideal
579 approach to link synapse ultrastructure and function in intact circuits of genetically defined neurons.

581 **Acknowledgements**

582 The authors wish to thank the following colleagues for their help with this work: Stefanie Esmond and Bridget
583 Kajs for rAAV preparation; Geoff Dilly, Melissa Burks, Molly O’Gara for stereotaxic rAAV injections; John
584 Mendenhall for help with EM and useful discussions on labeling strategies; Dan Johnston for use of a Zeiss
585 light microscope and helpful discussions on electrophysiology; Nuno de Costa (Allen Institute for Brain
586 Science) for Ni-DAB protocol; Jung-Hwa Tao-Cheng (NINDS Electron Microscopy Facility) for suggesting the
587 use gold enhancement; Patrick Parker for help in preparing this manuscript. All are at the University of Texas
588 at Austin unless otherwise noted. The authors also acknowledge the following funding sources: Brain
589 Research Foundation Scientific Innovations Award (to K.M.H.), NSF Grant (1707356 to K.M.H.), NIH Grants
590 (MH095980, R56MH095980, MH104319 and NS074644 to K.M.H.; EY026446, EY026442, and NS094330 to
591 B.V.Z.), Human Frontier Science Program (RGP0041 to B.V.Z.), and The University of Texas System UT
592 BRAIN Seed Grants (NNRI 365222 and 365289 to B.V.Z.).

References

1. Bourne JN, Harris KM. Coordination of size and number of excitatory and inhibitory synapses results in a balanced structural plasticity along mature hippocampal CA1 dendrites during LTP. *Hippocampus*. 2011;21: 354–373. doi:10.1002/hipo.20768
2. Ostroff LE, Fiala JC, Allwardt B, Harris KM. Polyribosomes Redistribute from Dendritic Shafts into Spines with Enlarged Synapses during LTP in Developing Rat Hippocampal Slices. *Neuron*. 2002;35: 535–545. doi:10.1016/S0896-6273(02)00785-7
3. Popov VI, Davies HA, Rogachevsky VV, Patrushev IV, Errington ML, Gabbott PLA, et al. Remodelling of synaptic morphology but unchanged synaptic density during late phase long-term potentiation(ltp): A serial section electron micrograph study in the dentate gyrus in the anaesthetised rat. *Neuroscience*. 2004;128: 251–262. doi:10.1016/j.neuroscience.2004.06.029
4. Smith HL, Bourne JN, Cao G, Chirillo MA, Ostroff LE, Watson DJ, et al. Mitochondrial support of persistent presynaptic vesicle mobilization with age-dependent synaptic growth after LTP. *eLife*. 2016;5: e15275. doi:10.7554/eLife.15275
5. Martell JD, Deerinck TJ, Sancak Y, Poulos TL, Mootha VK, Sosinsky GE, et al. Engineered ascorbate peroxidase as a genetically encoded reporter for electron microscopy. *Nat Biotechnol*. 2012;30: 1143–1148. doi:10.1038/nbt.2375
6. Lam SS, Martell JD, Kamer KJ, Deerinck TJ, Ellisman MH, Mootha VK, et al. Directed evolution of APEX2 for electron microscopy and proximity labeling. *Nat Methods*. 2015;12: 51–54. doi:10.1038/nmeth.3179
7. Nabavi S, Fox R, Proulx CD, Lin JY, Tsien RY, Malinow R. Engineering a memory with LTD and LTP. *Nature*. 2014;511: 348–352. doi:10.1038/nature13294
8. Oishi N, Nomoto M, Ohkawa N, Saitoh Y, Sano Y, Tsujimura S, et al. Artificial association of memory events by optogenetic stimulation of hippocampal CA3 cell ensembles. *Mol Brain*. 2019;12: 2. doi:10.1186/s13041-018-0424-1
9. Chun S, Bayazitov IT, Blundon JA, Zakharenko SS. Thalamocortical Long-Term Potentiation Becomes Gated after the Early Critical Period in the Auditory Cortex. *J Neurosci*. 2013;33: 7345–7357. doi:10.1523/JNEUROSCI.4500-12.2013

- 620 10. Hashimotodani Y, Nasrallah K, Jensen KR, Chávez AE, Carrera D, Castillo PE. LTP at Hilar Mossy Cell-
621 Dentate Granule Cell Synapses Modulates Dentate Gyrus Output by Increasing Excitation/Inhibition
622 Balance. *Neuron*. 2017;95: 928-943.e3. doi:10.1016/j.neuron.2017.07.028
- 623 11. Kohl MM, Shipton OA, Deacon RM, Rawlins JNP, Deisseroth K, Paulsen O. Hemisphere-specific
624 optogenetic stimulation reveals left-right asymmetry of hippocampal plasticity. *Nat Neurosci*. 2011;14:
625 1413–1415. doi:10.1038/nn.2915
- 626 12. Zhang Y-P, Oertner TG. Optical induction of synaptic plasticity using a light-sensitive channel. *Nat*
627 *Methods*. 2007;4: 139–141. doi:10.1038/nmeth988
- 628 13. O’Riordan KJ, Hu N-W, Rowan MJ. A β Facilitates LTD at Schaffer Collateral Synapses Preferentially in
629 the Left Hippocampus. *Cell Rep*. 2018;22: 2053–2065. doi:10.1016/j.celrep.2018.01.085
- 630 14. Berndt A, Schoenenberger P, Mattis J, Tye KM, Deisseroth K, Hegemann P, et al. High-efficiency
631 channelrhodopsins for fast neuronal stimulation at low light levels. *Proc Natl Acad Sci*. 2011;108: 7595–
632 7600. doi:10.1073/pnas.1017210108
- 633 15. Pédelacq J-D, Cabantous S, Tran T, Terwilliger TC, Waldo GS. Engineering and characterization of a
634 superfolder green fluorescent protein. *Nat Biotechnol*. 2006;24: 79–88. doi:10.1038/nbt1172
- 635 16. Stockklausner C, Ludwig J, Ruppertsberg JP, Klöcker N. A sequence motif responsible for ER export and
636 surface expression of Kir2.0 inward rectifier K⁺ channels. *FEBS Lett*. 2001;493: 129–133.
637 doi:10.1016/S0014-5793(01)02286-4
- 638 17. Mittler R, Zilinskas BA. Molecular cloning and nucleotide sequence analysis of a cDNA encoding pea
639 cytosolic ascorbate peroxidase. *FEBS Lett*. 1991;289: 257–259. doi:10.1016/0014-5793(91)81083-K
- 640 18. Moriyoshi K, Richards LJ, Akazawa C, O’Leary DDM, Nakanishi S. Labeling Neural Cells Using
641 Adenoviral Gene Transfer of Membrane-Targeted GFP. *Neuron*. 1996;16: 255–260. doi:10.1016/S0896-
642 6273(00)80044-6
- 643 19. Kim JH, Lee S-R, Li L-H, Park H-J, Park J-H, Lee KY, et al. High Cleavage Efficiency of a 2A Peptide
644 Derived from Porcine Teschovirus-1 in Human Cell Lines, Zebrafish and Mice. *PLOS ONE*. 2011;6:
645 e18556. doi:10.1371/journal.pone.0018556

- 646 20. Borghuis BG, Tian L, Xu Y, Nikonov SS, Vardi N, Zemelman BV, et al. Imaging Light Responses of
647 Targeted Neuron Populations in the Rodent Retina. *J Neurosci.* 2011;31: 2855–2867.
648 doi:10.1523/JNEUROSCI.6064-10.2011
- 649 21. Grieger JC, Choi VW, Samulski RJ. Production and characterization of adeno-associated viral vectors.
650 *Nat Protoc.* 2006;1: 1412–1428. doi:10.1038/nprot.2006.207
- 651 22. Aurnhammer C, Haase M, Muether N, Hausl M, Rauschhuber C, Huber I, et al. Universal Real-Time PCR
652 for the Detection and Quantification of Adeno-Associated Virus Serotype 2-Derived Inverted Terminal
653 Repeat Sequences. *Hum Gene Ther Methods.* 2012;23: 18–28. doi:10.1089/hgtb.2011.034
- 654 23. Yuste R, Miller RB, Holthoff K, Zhang S, Miesenböck G. Synapto-pHluorins: Chimeras between pH-
655 sensitive mutants of green fluorescent protein and synaptic vesicle membrane proteins as reporters of
656 neurotransmitter release. In: Thorner J, Emr SD, Abelson JN, editors. *Methods in Enzymology.* Academic
657 Press; 2000. pp. 522–546. doi:10.1016/S0076-6879(00)27300-X
- 658 24. Bourne JN, Kirov SA, Sorra KE, Harris KM. Warmer preparation of hippocampal slices prevents synapse
659 proliferation that might obscure LTP-related structural plasticity. *Neuropharmacology.* 2007;52: 55–59.
660 doi:10.1016/j.neuropharm.2006.06.020
- 661 25. Bourne JN, Harris KM. Nanoscale analysis of structural synaptic plasticity. *Curr Opin Neurobiol.* 2012;22:
662 372–382. doi:10.1016/j.conb.2011.10.019
- 663 26. Harris KM, Teyler TJ. Developmental onset of long-term potentiation in area CA1 of the rat hippocampus.
664 *J Physiol.* 1984;346: 27–48. doi:10.1113/jphysiol.1984.sp015005
- 665 27. Jensen FE, Harris KM. Preservation of neuronal ultrastructure in hippocampal slices using rapid
666 microwave-enhanced fixation. *J Neurosci Methods.* 1989;29: 217–230. doi:10.1016/0165-0270(89)90146-
667 5
- 668 28. Harris KM, Perry E, Bourne J, Feinberg M, Ostroff L, Hurlburt J. Uniform Serial Sectioning for
669 Transmission Electron Microscopy. *J Neurosci.* 2006;26: 12101–12103. doi:10.1523/JNEUROSCI.3994-
670 06.2006
- 671 29. Kuwajima M, Mendenhall JM, Harris KM. Large-Volume Reconstruction of Brain Tissue from High-
672 Resolution Serial Section Images Acquired by SEM-Based Scanning Transmission Electron Microscopy.

- 673 In: Sousa AA, Kruhlak MJ, editors. Nanoimaging. Humana Press; 2013. pp. 253–273. doi:10.1007/978-1-
674 62703-137-0_15
- 675 30. Reynolds ES. The use of lead citrate at high pH as an electron-opaque stain in electron microscopy. *J*
676 *Cell Biol.* 1963;17: 208–212.
- 677 31. Kuwajima M, Mendenhall JM, Lindsey LF, Harris KM. Automated Transmission-Mode Scanning Electron
678 Microscopy (tSEM) for Large Volume Analysis at Nanoscale Resolution. *PLoS ONE.* 2013;8: e59573.
679 doi:10.1371/journal.pone.0059573
- 680 32. Schindelin J, Arganda-Carreras I, Frise E, Kaynig V, Longair M, Pietzsch T, et al. Fiji: an open-source
681 platform for biological-image analysis. *Nat Methods.* 2012;9: 676–682. doi:10.1038/nmeth.2019
- 682 33. Cardona A, Saalfeld S, Schindelin J, Arganda-Carreras I, Preibisch S, Longair M, et al. TrakEM2
683 Software for Neural Circuit Reconstruction. *PLoS ONE.* 2012;7: e38011.
684 doi:10.1371/journal.pone.0038011
- 685 34. Saalfeld S, Fetter R, Cardona A, Tomancak P. Elastic volume reconstruction from series of ultra-thin
686 microscopy sections. *Nat Methods.* 2012;9: 717–720. doi:10.1038/nmeth.2072
- 687 35. Fiala JC. Reconstruct: a free editor for serial section microscopy. *J Microsc.* 2005;218: 52–61.
688 doi:10.1111/j.1365-2818.2005.01466.x
- 689 36. Fiala JC, Harris KM. Cylindrical diameters method for calibrating section thickness in serial electron
690 microscopy. *J Microsc.* 2001;202: 468–472. doi:10.1046/j.1365-2818.2001.00926.x
- 691 37. Fiala JC, Harris KM. Extending Unbiased Stereology of Brain Ultrastructure to Three-dimensional
692 Volumes. *J Am Med Inform Assoc.* 2001;8: 1–16. doi:10.1136/jamia.2001.0080001
- 693 38. Cao G, Harris KM. Developmental regulation of the late phase of long-term potentiation (L-LTP) and
694 metaplasticity in hippocampal area CA1 of the rat. *J Neurophysiol.* 2012;107: 902–912.
695 doi:10.1152/jn.00780.2011
- 696 39. Isomura Y, Fujiwara-Tsukamoto Y, Imanishi M, Nambu A, Takada M. Distance-Dependent Ni²⁺-
697 Sensitivity of Synaptic Plasticity in Apical Dendrites of Hippocampal CA1 Pyramidal Cells. *J Neurophysiol.*
698 2002;87: 1169–1174. doi:10.1152/jn.00536.2001

- 699 40. Kloosterman F, Peloquin P, Leung LS. Apical and Basal Orthodromic Population Spikes in Hippocampal
700 CA1 In Vivo Show Different Origins and Patterns of Propagation. *J Neurophysiol.* 2001;86: 2435–2444.
701 doi:10.1152/jn.2001.86.5.2435
- 702 41. Leung LW. Potentials evoked by alvear tract in hippocampal CA1 region of rats. I. Topographical
703 projection, component analysis, and correlation with unit activities. *J Neurophysiol.* 1979;42: 1557–1570.
704 doi:10.1152/jn.1979.42.6.1557
- 705 42. Wheal HV, Lancaster B, Bliss TVP. Long-term potentiation in Schaffer collateral and commissural
706 systems of the hippocampus: In vitro study in rats pretreated with kainic acid. *Brain Res.* 1983;272: 247–
707 253. doi:10.1016/0006-8993(83)90570-X
- 708 43. Jackman SL, Beneduce BM, Drew IR, Regehr WG. Achieving High-Frequency Optical Control of Synaptic
709 Transmission. *J Neurosci.* 2014;34: 7704–7714. doi:10.1523/JNEUROSCI.4694-13.2014
- 710 44. Zakharenko SS, Zablow L, Siegelbaum SA. Visualization of changes in presynaptic function during long-
711 term synaptic plasticity. *Nat Neurosci.* 2001;4: 711. doi:10.1038/89498
- 712 45. Hainfeld JF, Powell RD. New Frontiers in Gold Labeling. *J Histochem Cytochem.* 2000;48: 471–480.
713 doi:10.1177/002215540004800404
- 714 46. Bourne JN, Chirillo MA, Harris KM. Presynaptic Ultrastructural Plasticity Along CA3→CA1 Axons During
715 Long-Term Potentiation in Mature Hippocampus. *J Comp Neurol.* 2013;521: 3898–3912.
716 doi:10.1002/cne.23384
- 717 47. Shinohara Y, Hirase H, Watanabe M, Itakura M, Takahashi M, Shigemoto R. Left-right asymmetry of the
718 hippocampal synapses with differential subunit allocation of glutamate receptors. *Proc Natl Acad Sci.*
719 2008;105: 19498–19503. doi:10.1073/pnas.0807461105
- 720 48. Bliss TV, Lancaster B, Wheal HV. Long-term potentiation in commissural and Schaffer projections to
721 hippocampal CA1 cells: an in vivo study in the rat. *J Physiol.* 1983;341: 617–626.
722 doi:10.1113/jphysiol.1983.sp014828
- 723 49. Martin SJ, Shires KL, da Silva BM. Hippocampal Lateralization and Synaptic Plasticity in the Intact Rat:
724 No Left–Right Asymmetry in Electrically Induced CA3-CA1 Long-Term Potentiation. *Neuroscience.*
725 2019;397: 147–158. doi:10.1016/j.neuroscience.2018.11.044

- 726 50. Habib D, Dringenberg HC. Low-frequency-induced synaptic potentiation: A paradigm shift in the field of
727 memory-related plasticity mechanisms? *Hippocampus*. 2010;20: 29–35. doi:10.1002/hipo.20611
- 728 51. Magee JC, Johnston D. A Synaptically Controlled, Associative Signal for Hebbian Plasticity in
729 Hippocampal Neurons. *Science*. 1997;275: 209–213. doi:10.1126/science.275.5297.209
- 730 52. Markram H, Lübke J, Frotscher M, Sakmann B. Regulation of Synaptic Efficacy by Coincidence of
731 Postsynaptic APs and EPSPs. *Science*. 1997;275: 213–215. doi:10.1126/science.275.5297.213
- 732 53. Bortolotto ZA, Collingridge GL. Characterisation of LTP induced by the activation of glutamate
733 metabotropic receptors in area CA1 of the hippocampus. *Neuropharmacology*. 1993;32: 1–9.
734 doi:10.1016/0028-3908(93)90123-K
- 735 54. Kang H, Schuman EM. Long-lasting neurotrophin-induced enhancement of synaptic transmission in the
736 adult hippocampus. *Science*. 1995;267: 1658–1662. doi:10.1126/science.7886457
- 737 55. Lee J, Song EK, Bae Y, Min J, Rhee H-W, Park TJ, et al. An enhanced ascorbate peroxidase 2/antibody-
738 binding domain fusion protein (APEX2-ABD) as a recombinant target-specific signal amplifier. *Chem*
739 *Commun*. 2015;51: 10945–10948. doi:10.1039/C5CC02409A
- 740 56. Coleman RA, Liu J, Wade JB. Use of anti-fluorophore antibody to achieve high-sensitivity
741 immunolocalizations of transporters and ion channels. *J Histochem Cytochem Off J Histochem Soc*.
742 2006;54: 817–827. doi:10.1369/jhc.6A6929.2006
- 743 57. Oberti D, Kirschmann MA, Hahnloser RHR. Correlative microscopy of densely labeled projection neurons
744 using neural tracers. *Front Neuroanat*. 2010;4: 24. doi:10.3389/fnana.2010.00024
- 745 58. Paxinos G, Franklin KBJ. *The Mouse Brain in Stereotaxic Coordinates*. 2nd edition. San Diego: Academic
746 Press; 2001.
- 747

Supporting information

S1 Fig. Verification of rAAV injections and further characterization of oEPSP at CA3→CA1 synapses.

(A-B) Unilateral injections of rAAV into the area CA3 result in GFP labeling of Schaffer collaterals and commissural fibers. (A) A diagram (modified from ref. 58) showing the approximate site of rAAV injection site in the mouse hippocampal area CA3. An infected CA3 neuron (green) on the right hemisphere depicted under the injection needle (magenta) projects its axons to synapse onto neurons in both ipsilateral and contralateral CA1 via Schaffer collaterals and commissural fibers, respectively. These axons can also synapse onto uninfected CA3 neurons (black). (B) A montage of two epifluorescence images of a coronal section through the injection site in the right area CA3. The right hemisphere (injected side) was partially damaged during extraction of the brain. Scale bar = 1 mm. (C-F) In acute transverse slices of the hippocampus prepared from rAAV injected mice, light pulse stimulation of the virally targeted CA3 axons evoked oEPSPs in the area CA1. (C) Example traces of oEPSPs recorded from an electrode positioned in different CA1 layers (colored circles): strata oriens (SO), pyramidale (SP), radiatum (SR), and lacunosum-moleculare (SLM). Optical fiber was placed in SR in the proximal area CA1, ~400 μ m from the recording electrode. Scale bars = 5 ms, 1 mV. (D) Amplitude (left) and slope (right) of optically and electrically evoked field EPSPs. Optical stimulation was delivered at the maximum light intensity, while electrical stimulation was at half-maximum. Horizontal lines and error bars indicate mean \pm SEM. The number of slices used for each condition is indicated in parentheses. (E) Optical paired-pulse stimulation induces slight facilitation (mean \pm SEM, n = 6 slices). Scale bars = 10 ms, 1 mV. (F) oEPSP was blocked by application of 1 μ M TTX (left) or by 20 μ M DNQX (right). Scale bars = 5 ms, 1 mV (TTX); 5 ms, 2 mV (NBQX). The recordings shown in D-F were made from the middle SR.

S2 Fig. Input-output (IO) curves recorded from the area CA1 in intact and cut slices. (A) Representative oEPSP traces recorded from a slice with intact CA3. (B) Same as A, but recorded from a cut slice. Scale bars = 1 ms, 1 mV for A and B. (C) Optical IO curves recorded from intact and cut slices. The intensities of light stimulation used to record optical IO: 30% (~4 mW), 60% (~9mW), 90% (~13mW), and 100% (~14.5 mW). There is no significant difference between responses evoked by 90% and 100% light intensities (t = 0.317, df = 10, p > 0.05 for intact slices; t = 0.342, df = 9, p > 0.05 for cut slices; two-sided paired t-test). (D) Summary of

775 oEPSP slope (left) and amplitude (right) recorded at the maximum light power. **(E)** Input-output curves
776 recorded using an electrical stimulation. **(F)** Summary of eEPSP slope (left) and amplitude (right) recorded at
777 intensity that resulted in approximately half-maximum slope. All graphs **(C-F)** show mean \pm SEM. Different sets
778 of slices were analyzed for **C** and **D**; **E** and **F**. The number of slices used for each condition is indicated in
779 parentheses.

781 **S3 Fig. Enzymatic activity of mAPEX is preserved after chemical fixation with glutaraldehyde.**

782 Diaminobenzidine (DAB) was used as a substrate because autofluorescence from glutaraldehyde makes it
783 difficult to assess labeling with tyramide-conjugated fluorescent dyes. **(A)** Right: mAPEX1 expressed in
784 dissociated rat hippocampal neurons, fixed with 6% glutaraldehyde and 2% formaldehyde, were capable of
785 generating the dark brown DAB reaction product. Left: Control neurons fixed and treated with DAB in the same
786 manner did not exhibit the reaction product. Scale bars = 50 μ m. **(B)** Two serial tSEM images showing axons
787 labeled with Ni-enhanced DAB (red contours) through the area CA1 from a perfusion-fixed C57B/6J mouse.
788 The rAAV was injected into the ipsilateral hippocampal area CA1 to express mAPEX2. The fixative contained
789 2.5% glutaraldehyde and 2% formaldehyde. Scale bars = 500 nm. Insets: Enlarged areas indicated by black
790 rectangles. Electron-dense Ni-DAB reaction product obscures subcellular structures in the labeled axons. In
791 contrast, small synaptic vesicles are visible in an unlabeled axonal bouton nearby (ax). Scale bars = 100 nm.

792
793 **S4 Fig. Electron-dense artifacts and subcellular structures present in unlabeled sections.** Electron-
794 dense artifacts and subcellular structures present in unlabeled sections. Five serial tSEM images from the
795 series presented in Fig 3C. These images were acquired from serial thin sections that were not immunolabeled
796 for Alexa Fluor dye, but stained with uranyl acetate and lead citrate (UA/Pb) prior to tSEM imaging. While
797 glycogen granules fill glial processes (green arrowheads in 'g'), they are less common in axons (ax) and
798 boutons (b1, b2, and b3) and do not appear in the same profiles over two consecutive sections (yellow
799 arrowheads). Post-section staining with UA/Pb can be a source of electron-dense artifacts of various size and
800 shape (purple arrowheads) that are usually confined to single sections. On rare occasions, small artifacts could
801 appear in two consecutive sections. However, their small size (diameter \leq 10 nm) is similar to those generated

802 as a result of background nucleation during gold enhancement (see S5 Fig), and therefore, can easily be
803 distinguished from positive labeling should they also occur in immunolabeled sections. Scale bar = 250 nm.

804
805 **S5 Fig. Electron-dense artifacts due to gold enhancement reagent. Electron-dense artifacts due to gold**
806 **enhancement reagent. (A)** A histogram showing the distribution of diameters of gold-enhanced gold particles
807 (bin size = 2 nm). A total of 527 particles were analyzed with Fiji software (see Materials and methods). Their
808 diameter ranged from 2.5 nm to 85.3 nm with the median of 37.1 nm and the mean of 36.5 ± 0.61 nm (SEM). A
809 vertical line at 10 nm indicates the cutoff for gold particles excluded during identification of labeled axons. **(B)** A
810 tSEM image acquired from serial thin sections that were not immunolabeled, but incubated with the gold
811 enhancement reagent and then stained with uranyl acetate and lead citrate. Small electron-dense particles
812 (indicated by dotted red circles) were 10 nm or smaller in diameter, and were present in dendrites (den), axons
813 (ax), and boutons (b). These small particles likely formed as a result of self-nucleation of gold enhancement
814 reagent, and therefore were excluded during identification of labeled axons. Scale bar = 250 nm.

815
816 **S1 Video. A video of the reconstructed axon shown in Fig 4.** File name: S1_video.mp4. File size: 71.1 MB.

817 This video is also available as an external file – see Data Availability.

